

High-Coherence Quantum Acoustics with Planar Superconducting Qubits

W.J.M. Franse,¹ C.A. Potts,^{1,2,3} V.A.S.V. Bittencourt,⁴ A. Metelmann,^{4,5} and G.A. Steele^{1,*}

¹*Kavli Institute of NanoScience, Delft University of Technology, PO Box 5046, 2600 GA Delft, Netherlands*

²*Niels Bohr Institute, University of Copenhagen, Blegdamsvej 17, 2100 Copenhagen, Denmark*

³*Center for Hybrid Quantum Networks (Hy-Q), Niels Bohr Institute, University of Copenhagen, Copenhagen, Denmark*

⁴*ISIS (UMR 7006), Université de Strasbourg, 67000 Strasbourg, France*

⁵*Institute for Theory of Condensed Matter and Institute for Quantum Materials and Technology, Karlsruhe Institute of Technology, 76131, Karlsruhe, Germany*

(Dated: October 15, 2024)

Quantum acoustics is an emerging platform for hybrid quantum technologies enabling quantum coherent control of mechanical vibrations. High-overtone bulk acoustic resonators (HBARs) represent an attractive mechanical implementation of quantum acoustics due to their potential for exceptionally high mechanical coherence. Here, we demonstrate an implementation of high-coherence HBAR quantum acoustics integrated with a planar superconducting qubit architecture, demonstrating an acoustically-induced-transparency regime of high cooperativity and weak coupling, analogous to the electrically-induced transparency in atomic physics. Demonstrating high-coherence quantum acoustics with planar superconducting devices enables new applications for acoustic resonators in quantum technologies.

In the field of quantum acoustodynamics (cQAD), superconducting transmon qubits [1–3] have been coupled to multiple different forms of mechanical modes such as propagating surface acoustic (SAW) [4–7], film bulk acoustic resonators (FBARs) [8], ultra-high-frequency (UHF) nanoresonator [9], nanomechanical resonators [10, 11] and high-overtone bulk acoustic resonator (HBAR) coupled to either 3D [12–14] or 2D transmons [15–18]. The potential applications of HBAR quantum acoustic devices include compact quantum memories [19], quantum interfaces to spin devices [20, 21], microwave to optical quantum transduction [22], and the exploration of fundamental mass limits in quantum mechanics [23, 24].

An attractive feature of HBARs is the small surface-to-volume ratio of the acoustic modes, enabling them to exploit the exceptionally high bulk mechanical quality factor of crystalline materials, with bulk modes whose quality factor can exceed 10^{10} [25]. While the pioneering work [12] with HBARs achieved moderate quality factors of 10^5 , quality factors of 10^6 were soon achieved [13, 26] by shaping the top piezo element to reduce diffraction by shaping the acoustic mode, creating an effective acoustic plano-convex lens.

Initial work in the field focused on superconducting qubits in 3D architecture, which enables high coherence times of the superconducting qubit [12]. While it can be more difficult to engineer the same coherence times in planar qubit devices, the planar approach offers significant advantages, such as the ease of integrating multiple qubits on the same chip. The planar design also enables the inclusion of fast-flux lines for rapid control of qubit frequencies and qubit couplings and enables high-speed parametric modulation for applications such as parametric amplifiers and on-chip circulators [27]. The integra-

tion of acoustic devices with planar superconducting circuits would provide a valuable new quantum resource, but until now, attempts to integrate HBARs with planar circuits have resulted in reduced coherence of the mechanical modes [15, 17] exhibiting quality factors on the order of 10^3 to 10^4 .

Here, we demonstrate the integration of HBAR devices with state-of-the-art mechanical coherence with a planar superconducting qubit chip. Our architecture is

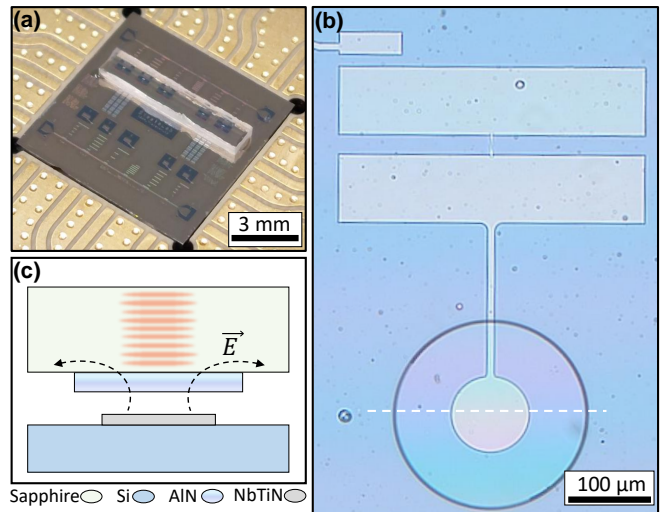


FIG. 1. A planar Transmon flip-chip HBAR device. (a) Photo of the assembled device. (b) Optical image of transmon with HBAR on top. White light interference fringes in HBAR suggest a gap distance of a few micrometers between the top and bottom chip. (c) Schematic side view of assembly drawn at the dashed white line in (b). The antenna of the transmon qubit emits an alternating electric field, \vec{E} , to actuate the piezoelectric, which in turn generates a standing wave in the sapphire substrate.

* g.a.steele@tudelft.nl

based on a flip-chip assembly of a piezoelectric HBAR chip on top of a superconducting qubit chip fabricated on a silicon wafer using standard circuit QED processes and designs. We observe sharp HBAR resonances inside a broad qubit linewidth, whose mechanical nature is confirmed by changing the qubit frequency through multiple resonances via AC-Stark tuning with a nearby drive tone. To decouple the effect of the hybridization of the HBAR mode with the qubit, the resulting lineshapes are analyzed using a master equation simulation to extract the intrinsic mechanical damping rate [28]. Doing so, we extract intrinsic damping rates 6.8 kHz, corresponding to Q-factors of 9.0×10^5 , despite the absence of any mechanical lensing engineered in the piezo actuation layer, promising for the integration of HBARS with more complex superconducting circuits for applications in quantum technologies.

The device has two feedlines with five multiplexed readout resonators coupled to five niobium-titanium nitride transmon qubits. The top line has the flipped HBAR chip aligned with the transmon qubits, and the bottom line is an exact copy without the HBAR chip for control measurements. In this flip-chip architecture, the top chip consists of five cylindrical-shaped aluminum nitride piezoelectric transducers on a sapphire substrate. The bottom chip includes superconducting transmons and coplanar waveguide readout resonators on a silicon substrate; see Fig. 1(a,c). An optical micrograph of a single transmon qubit with an HBAR is shown in Fig. 1(b); the piezoelectric cylinder is visible as a large circle exhibiting white light interference. The interference pattern suggests a gap between the piezoelectric disk and the silicon substrate on the order of $1 \mu\text{m}$.

To excite HBAR modes near 6 GHz most efficiently, the piezoelectric layer was designed to have a thickness of $t_p \approx 900 \text{ nm}$. Since the resonance frequency of the piezoelectric disk is given by $f_0 = v_p/2t_p$, where v_p is the acoustic velocity in the piezoelectric material ($v_{\text{AIN}} \approx 1.14 \times 10^4 \text{ m/s}$). The mode spacing between two consecutive resonances, the free spectral range (FSR), of the phononic resonator, is given by $f_{\text{FSR}} = v_s/2t_s$, where v_s is the acoustic velocity in sapphire ($\sim 1.11 \times 10^4 \text{ m/s}$) and t_s the HBAR thickness, with a predicted FSR of 8.538 MHz for a $650 \mu\text{m}$ sapphire substrate.

The flip-chip device was cooled to a temperature of $\sim 20 \text{ mK}$ in a commercial dilution refrigerator. We measured our readout resonator $\omega_r = 2\pi \times 4.910 \text{ GHz}$ to be 1.07 GHz detuned from our qubit's ground-to-excited state transition frequency $\omega_{\text{eg}} = 2\pi \times 6.067 \text{ GHz}$. To confirm coupling to HBAR resonances, we use the AC-Stark effect [29–31] to shift the qubit's resonance frequency. The Stark drive was applied to the qubit detuned 30 MHz above the qubit frequency, $\omega_{\text{Stark}} = 2\pi \times 6.09605 \text{ GHz}$. Increasing the Stark tone's power while performing two-tone spectroscopy shifts the qubit to lower frequencies; see Fig. 2. In this measurement, a high-power qubit probe tone is applied such that power broadening allows the simultaneous measurement of multiple HBAR reso-

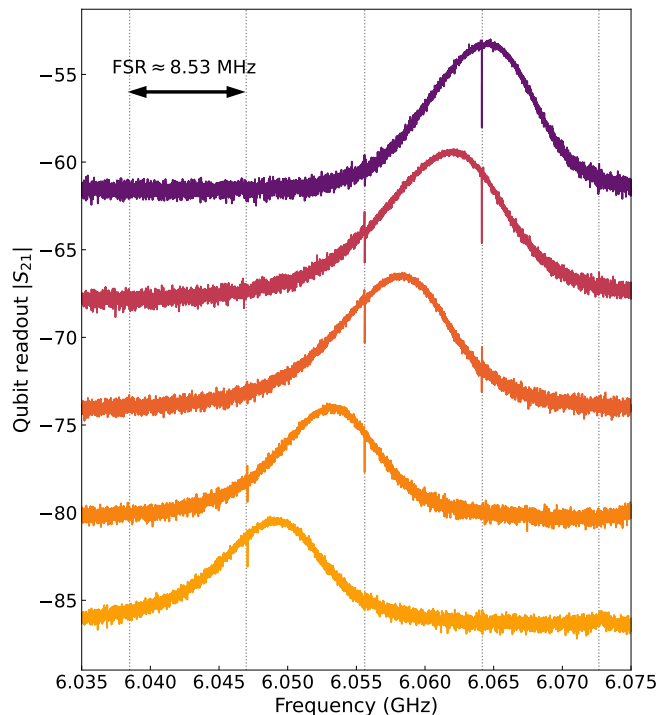


FIG. 2. Observation of multiple HBAR resonances by AC-Stark shifting of the qubit frequency. The qubit $\omega_{\text{eg}}/2\pi$ transition is tuned using a Stark drive tone with small detuning ($\omega_{\text{Stark}}/2\pi = 6.09605 \text{ GHz}$). The curves represent two-tone spectroscopy measurements for different Stark powers (top to bottom: -22.0, -15.5, -12.0, -9.0, -7.5 dBm). HBAR resonances are observed at fixed frequencies separated by a free spectral range of 8.53 MHz, corresponding to a $650 \mu\text{m}$ Sapphire substrate.

nances within the qubit linewidth. The sharp resonances occur every 8.53 MHz, in excellent agreement with the designed FSR.

In order to quantify the interaction strength of the qubit and the phonon modes, additional two-tone spectroscopy was performed with sufficient resonator probe power and qubit drive power so that only one acoustic mode became visible within the qubit peak. To optimize measurement time, we performed segmented qubit drive frequency sweeps: In a span of 200 kHz around the acoustic mode, frequency points were spaced 250 Hz apart, but in a larger span of 20 MHz around the qubit ω_{eg} transition, they were spaced 250 kHz apart. The data (grey dots) is shown in Fig. 3, where panel (a) shows full acoustically-induced transparency (AIT) of qubit with one coupled acoustic mode and (b) shows a zoom-in of the HBAR mode.

Figure 3 shows high-resolution traces of the HBAR AIT resonances observed in qubit spectroscopy taken at low qubit drive and readout resonator drive powers to minimize the broadening of the qubit linewidth. Panel (a) shows a wide sweep in this regime, where the full qubit peak is visible. The qubit spectroscopic peak shows a small degree of asymmetry in its lineshape, which we

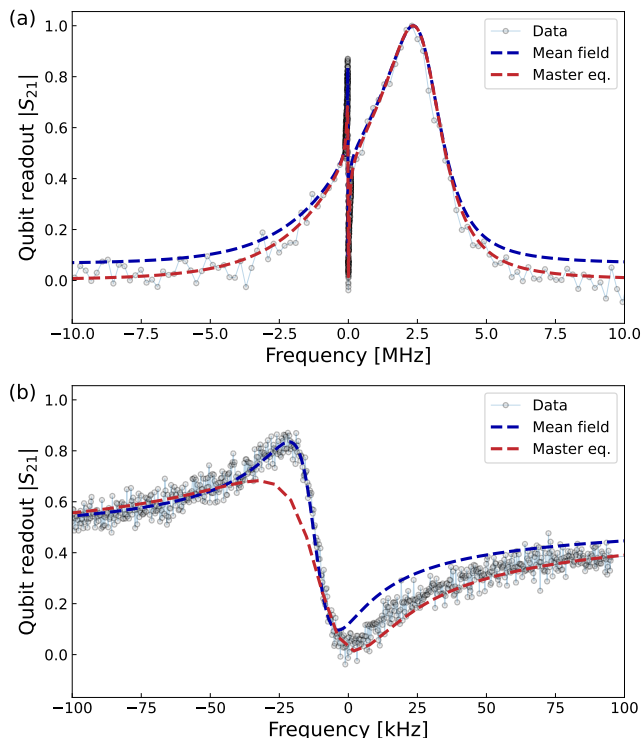


FIG. 3. Extracting the intrinsic mechanical damping rate in the AIT regime. (a) Experimental two-tone data of qubit ground-to-excited state transition coupled to a single HBAR mode at 6.064 GHz at low qubit driving power. Both panels also show the qubit spectrum determined from mean-field (blue dashed line) and master equation simulations (red dashed line). (b) Zoom in on the HBAR resonance. The fit to the mean-field theory determines an intrinsic mechanical damping rate of $\gamma/2\pi = 6.98 \pm 0.03$ kHz, corresponding to a quality factor of 9.0×10^5 , and a qubit-phonon coupling $g_{\text{qh}}/2\pi = 197 \pm 1$ kHz. In panels (a) and (b), frequency refers to the detuning from the HBAR mode.

attribute to the residual thermal occupation of the readout resonator; see Ref. [28]. The line indicates the result of a master equation and mean-field calculations of the qubit spectroscopy. The mean-field curve was used to extract the intrinsic damping rate of the mechanical mode by fitting the data. We note that even at low powers, the qubit has a relatively large linewidth of 425 kHz. While it is likely that dielectric losses from the piezoelectric can reduce qubit coherence, in our case, the reference qubits on the chip which were not coupled to the HBARs also showed comparable linewidths, suggesting the piezoelectric layer, in this case, is not the source of qubit decay. We currently believe that the large linewidth in our qubit fabrication process is related to an interaction of the aluminum layer of the qubit with a silicon layer that was overetched during the base layer patterning.

Figure 3(b) shows a zoom of the AIT feature with high spectral resolution along with the calculations. From the mean-field model, we extract an intrinsic mechanical damping rate of the HBAR mode of 6.98 ± 0.03 kHz,

describing the mechanical decay rate if the HBAR were decoupled from the qubit entirely, and a qubit-HBAR coupling rate of 197 ± 1 kHz. We note that the spectroscopic AIT feature observed in the experimental spectroscopy can be both broader than the intrinsic mechanical linewidth due to hybridization with the qubit but also narrower than the intrinsic mechanical linewidth at higher qubit drive powers due to mechanical amplification and narrowing stemming from single-atom lasing physics [28]. As described in previous work [28], there is good agreement between the calculation and the experiment. However, we can see here that the master equation simulations performed failed to capture a slight bump on the left side of the AIT feature. This feature can be captured better by mean-field calculations [28]. In any case, both mean-field and master equation modelling describes the behaviour of the data and can be used to extract similar line widths.

Interestingly, we achieved state-of-the-art mechanical coherence, comparable to the best HBARs in 3D qubit architectures, in the absence of any shaping of the piezo surface to produce acoustic lensing. It is interesting to ask why the etched piezo shaping is not needed on our device. One possibility is that the small qubit electrode combined with the large piezo disc may already provide some electrostatic lensing from the non-uniform electric fields in the piezoelectric material, something which could be explored in future work. The high coherence demonstrated here, in any case, opens up an exciting route to combining quantum acoustics with planar technologies such as fast flux lines, flux-mediated parametric gates [32], SNAILs [33], and asymmetrically threaded SQUIDs [34].

W.J.M.F and G.A.S. acknowledge support through the QUAKE project, project number 680.92.18.04, of the research programme Natuurkunde Vrije Programma's of the Dutch Research Council (NWO). C.A.P. acknowledges the support of the Natural Sciences and Engineering Research Council of Canada (NSERC). A.M. and V.A.S.V.B. acknowledge financial support from the Contrat Triennal 2021-2023 Strasbourg Capitale Européenne.

Authors contributions W.J.M.F. fabricated the device, performed experiments, and wrote the manuscript. V.A.S.V.B. performed theoretical modelling. C.A.P. performed experiments, theoretical modelling and provided supervision. A.M. provided supervision and funding acquisition. G.A.S. provided supervision, conceptualization and funding acquisition.

Competing interests: The authors declare no competing interests.

Data and materials availability All data, analysis code, and measurement software are available and provided at <https://doi.org/10.5281/zenodo.13881198> [35].

- [1] A. Wallraff, D. I. Schuster, A. Blais, L. Frunzio, J. Majer, M. H. Devoret, S. M. Girvin, and R. J. Schoelkopf, Approaching unit visibility for control of a superconducting qubit with dispersive readout, *Physical Review Letters* **95**, 10.1103/physrevlett.95.060501 (2005).
- [2] D. I. Schuster, A. A. Houck, J. A. Schreier, A. Wallraff, J. M. Gambetta, A. Blais, L. Frunzio, J. Majer, B. Johnson, M. H. Devoret, S. M. Girvin, and R. J. Schoelkopf, Resolving photon number states in a superconducting circuit, *Nature* **445**, 515 (2007).
- [3] J. Koch, T. M. Yu, J. Gambetta, A. A. Houck, D. I. Schuster, J. Majer, A. Blais, M. H. Devoret, S. M. Girvin, and R. J. Schoelkopf, Charge-insensitive qubit design derived from the cooper pair box, *Physical Review A* **76**, 10.1103/physreva.76.042319 (2007).
- [4] M. V. Gustafsson, T. Aref, A. F. Kockum, M. K. Ekström, G. Johansson, and P. Delsing, Propagating phonons coupled to an artificial atom, *Science* **346**, 207 (2014).
- [5] K. J. Satzinger, Y. P. Zhong, H.-S. Chang, G. A. Peairs, A. Bienfait, M.-H. Chou, A. Y. Cleland, C. R. Conner, É. Dumur, J. Grebel, I. Gutierrez, B. H. November, R. G. Povey, S. J. Whiteley, D. D. Awschalom, D. I. Schuster, and A. N. Cleland, Quantum control of surface acoustic-wave phonons, *Nature* **563**, 661 (2018).
- [6] A. Bienfait, K. J. Satzinger, Y. P. Zhong, H.-S. Chang, M.-H. Chou, C. R. Conner, É. Dumur, J. Grebel, G. A. Peairs, R. G. Povey, and A. N. Cleland, Phonon-mediated quantum state transfer and remote qubit entanglement, *Science* **364**, 368 (2019).
- [7] C. Undershute, J. M. Kitzman, C. A. Mikolas, and J. Pollanen, Decoherence of surface phonons in a quantum acoustic system, *arXiv preprint arXiv:2410.03005* (2024).
- [8] A. O’Connell, M. Hofheinz, M. Ansmann, R. Bialczak, M. Lenander, E. Lucero, M. Neeley, D. Sank, H. Wang, M. Weides, J. Wenner, J. Martinis, and A. Cleland, Quantum ground state and single-phonon control of a mechanical resonator, *Nature* **464**, 697 (2010).
- [9] F. Rouxinol, Y. Hao, F. Brito, A. O. Caldeira, E. K. Irish, and M. D. LaHaye, Measurements of nanoresonator-qubit interactions in a hybrid quantum electromechanical system, *Nanotechnology* **27**, 364003 (2016).
- [10] P. Arrangoiz-Arriola and A. H. Safavi-Naeini, Engineering interactions between superconducting qubits and phononic nanostructures, *Phys. Rev. A* **94**, 063864 (2016).
- [11] P. Arrangoiz-Arriola, E. A. Wollack, Z. Wang, M. Pechal, W. Jiang, T. P. McKenna, J. D. Witmer, R. V. Laer, and A. H. Safavi-Naeini, Resolving the energy levels of a nanomechanical oscillator, *Nature* **571**, 537 (2019).
- [12] Y. Chu, P. Kharel, W. H. Renninger, L. D. Burkhardt, L. Frunzio, P. T. Rakich, and R. J. Schoelkopf, Quantum acoustics with superconducting qubits, *Science* **358**, 199 (2017).
- [13] Y. Chu, P. Kharel, T. Yoon, L. Frunzio, P. T. Rakich, and R. J. Schoelkopf, Creation and control of multi-phonon fock states in a bulk acoustic-wave resonator, *Nature* **563**, 666 (2018).
- [14] V. Jain, V. D. Kurilovich, Y. D. Dahmani, C. U. Lei, D. Mason, T. Yoon, P. T. Rakich, L. I. Glazman, and R. J. Schoelkopf, Acoustic radiation from a superconducting qubit: From spontaneous emission to rabi oscillations, *Phys. Rev. Appl.* **20**, 014018 (2023).
- [15] M. Kervinen, I. Rissanen, and M. Sillanpää, Interfacing planar superconducting qubits with high overtone bulk acoustic phonons, *Physical Review B* **97**, 10.1103/physrevb.97.205443 (2018).
- [16] M. Kervinen, J. E. Ramí rez-Muñoz, A. Välimaa, and M. A. Sillanpää, Landau-zener-stückelberg interference in a multimode electromechanical system in the quantum regime, *Physical Review Letters* **123**, 10.1103/physrevlett.123.240401 (2019).
- [17] M. Kervinen, A. Välimaa, J. E. Ramí rez-Muñoz, and M. A. Sillanpää, Sideband control of a multimode quantum bulk acoustic system, *Physical Review Applied* **14**, 10.1103/physrevapplied.14.054023 (2020).
- [18] A. Välimaa, W. Crump, M. Kervinen, and M. A. Sillanpää, Multiphonon transitions in a quantum electromechanical system, *Phys. Rev. Appl.* **17**, 064003 (2022).
- [19] C. T. Hann, C.-L. Zou, Y. Zhang, Y. Chu, R. J. Schoelkopf, S. M. Girvin, and L. Jiang, Hardware-efficient quantum random access memory with hybrid quantum acoustic systems, *Physical review letters* **123**, 250501 (2019).
- [20] E. MacQuarrie, T. Gosavi, N. Jungwirth, S. Bhave, and G. Fuchs, Mechanical spin control of nitrogen-vacancy centers in diamond, *Physical review letters* **111**, 227602 (2013).
- [21] H. Chen, N. F. Opondo, B. Jiang, E. R. MacQuarrie, R. S. Daveau, S. A. Bhave, and G. D. Fuchs, Engineering electron-phonon coupling of quantum defects to a semiconfocal acoustic resonator, *Nano letters* **19**, 7021 (2019).
- [22] T. Blésin, H. Tian, S. A. Bhave, and T. J. Kippenberg, Quantum coherent microwave-optical transduction using high-overtone bulk acoustic resonances, *Physical Review A* **104**, 052601 (2021).
- [23] M. F. Gely and G. A. Steele, Superconducting electromechanics to test diósi-penrose effects of general relativity in massive superpositions, *AVS Quantum Science* **3**, 10.1116/5.0050988 (2021).
- [24] M. Bild, M. Fadel, Y. Yang, U. von Lüpke, P. Martin, A. Bruno, and Y. Chu, Schrödinger cat states of a 16-microgram mechanical oscillator, *Science* **380**, 274 (2023).
- [25] S. Galliou, M. Goryachev, R. Bourquin, P. Abbé, J. P. Aubry, and M. E. Tobar, Extremely low loss phonon-trapping cryogenic acoustic cavities for future physical experiments, *Scientific reports* **3**, 2132 (2013).
- [26] U. von Lüpke, Y. Yang, M. Bild, L. Michaud, M. Fadel, and Y. Chu, Parity measurement in the strong dispersive regime of circuit quantum acoustodynamics, *Nature Physics* **18**, 794 (2022).
- [27] R. Navarathna, D. T. Le, A. R. Hamann, H. D. Nguyen, T. M. Stace, and A. Fedorov, Passive superconducting circulator on a chip, *Physical review letters* **130**, 037001 (2023).
- [28] C. Potts, W. Franse, V. Bittencourt, A. Metelmann, and G. Steele, A superconducting single-atom phonon laser, *arXiv preprint arXiv:2312.13948* (2023).
- [29] M. Brune, P. Nussenzeig, F. Schmidt-Kaler, F. Bernar-

- dot, A. Maali, J. M. Raimond, and S. Haroche, From lamb shift to light shifts: Vacuum and subphoton cavity fields measured by atomic phase sensitive detection, *Phys. Rev. Lett.* **72**, 3339 (1994).
- [30] D. I. Schuster, A. Wallraff, A. Blais, L. Frunzio, R.-S. Huang, J. Majer, S. M. Girvin, and R. J. Schoelkopf, ac stark shift and dephasing of a superconducting qubit strongly coupled to a cavity field, *Physical Review Letters* **94**, 10.1103/physrevlett.94.123602 (2005).
- [31] J. Gambetta, A. Blais, D. I. Schuster, A. Wallraff, L. Frunzio, J. Majer, M. H. Devoret, S. M. Girvin, and R. J. Schoelkopf, Qubit-photon interactions in a cavity: Measurement-induced dephasing and number splitting, *Physical Review A* **74**, 10.1103/physreva.74.042318 (2006).
- [32] N. Didier, E. A. Sete, J. Combes, and M. P. da Silva, Ac flux sweet spots in parametrically modulated superconducting qubits, *Physical Review Applied* **12**, 054015 (2019).
- [33] V. Sivak, N. Frattini, V. Joshi, A. Lingenfelter, S. Shankar, and M. Devoret, Kerr-free three-wave mixing in superconducting quantum circuits, *Physical Review Applied* **11**, 054060 (2019).
- [34] R. Lescanne, M. Villiers, T. Peronin, A. Sarlette, M. Delbecq, B. Huard, T. Kontos, M. Mirrahimi, and Z. Leghtas, Exponential suppression of bit-flips in a qubit encoded in an oscillator, *Nature Physics* **16**, 509 (2020).
- [35] Code available at: (2024).
- [36] D. J. Thoen, B. G. C. Bos, E. A. F. Haalebos, T. M. Klapwijk, J. J. A. Baselmans, and A. Endo, Superconducting NbTiN thin films with highly uniform properties over a 100 mm wafer, *IEEE Transactions on Applied Superconductivity* **27**, 1 (2017).
- [37] J. Gambetta, A. Blais, M. Boissonneault, A. A. Houck, D. I. Schuster, and S. M. Girvin, Quantum trajectory approach to circuit qed: Quantum jumps and the zeno effect, *Phys. Rev. A* **77**, 012112 (2008).
- [38] J. Gambetta, A. Blais, D. I. Schuster, A. Wallraff, L. Frunzio, J. Majer, M. H. Devoret, S. M. Girvin, and R. J. Schoelkopf, Qubit-photon interactions in a cavity: Measurement-induced dephasing and number splitting, *Phys. Rev. A* **74**, 042318 (2006).

Supplemental Materials: High-Coherence Quantum Acoustics with Planar Superconducting Qubits

I. DEVICE FABRICATION

The transmon qubits were fabricated on a 10x10 mm 525 μm thick high resistivity $\langle 100 \rangle$ silicon chip with a 100 nm layer of niobium-titanium nitride (NbTiN). The NbTiN deposition step was performed by the Dutch Institute for Space Research (SRON) following the process described in Ref. [36]. A layer of photoresist (AR-P 6200.18, 4000 rpm) was exposed (EBPG 5200, 315 $\mu\text{m}/\text{cm}^2$) and developed (Pentylacetate, O-xylene, IPA) to form the bulk circuitry (transmon islands and coplanar waveguides). After patterning, the NbTiN was removed using a reactive ion etch (RIE) in the Sentech Etchlab 200 (13.5 sccm SF_6 + 5 sccm O_2 , 55 W, 10 μbar) followed by an in-situ oxygen descum (50 sccm O_2 , 100 W, 10 μbar). Following removal of the photoresist layer, a bilayer resist stack (MMA-MAA copolymer 8.5% EL6, 2000 rpm and P(MMA-MAA) copolymer A6 950k, 1500 rpm, baked for three and five minutes, respectively, at 180 $^\circ\text{C}$) was used for patterning the 190 nm wide Josephson junctions. The junctions were patterned by e-beam lithography using a dose of 1700 μCcm^{-2} . The bilayer was developed using cold $\text{H}_2\text{O}:\text{IPA}$ (1:3) and cleaned with IPA. After cleaning the exposed silicon surface with an oxygen descum (200 sccm, 100 W) and an acid clean (BoE(7:1): H_2O , 1:1), the chip was placed in an aluminum (Al) evaporator (Plassys MEB550). The Manhattan-style junctions were fabricated using a standard double-angle shadow evaporation technique with an intermediate in-situ oxidation. The aluminium was deposited at an angle of 35 $^\circ$ at 0 $^\circ$ and 90 $^\circ$ rotation. The bottom and top layers were 35 and 75 nm thick, respectively. After the first evaporation step, the electrodes were oxidized to create the AlO_x tunnel barriers and following the second deposition step to cap the junctions with a passivation layer. Following the liftoff of the bilayer resist in NMP, the qubit chip was completed. Fig. S1 above shows the step-by-step process just described.

The HBAR chip was fabricated using double-side polished 4" sapphire wafers; one side was coated with a 1 μm thick film of c-axis oriented AlN (Kyma technologies, AT.U.100.1000.B). The wafer was first diced into 10x10mm chips for easier processing. A photoresist layer (AR-N 4450.10, 6000 rpm) was used to pattern circular regions to mask off the AlN. The AlN disks were formed using a reactive ion etch (RIE) in an Oxford 100 etcher ($\text{Cl}_2/\text{BCl}_3/\text{Ar}$

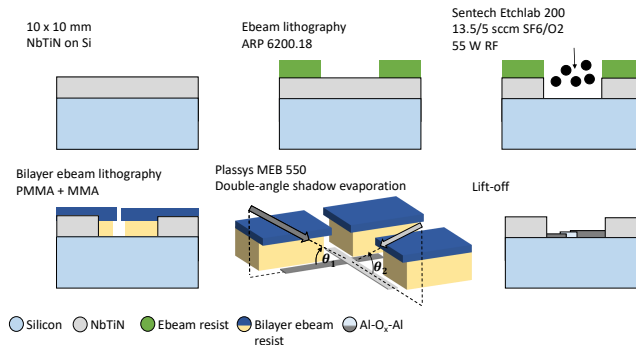


FIG. S1. **Fabrication transmon chip.** Drawings show a step-by-step process for fabricating our 2D transmon qubits. Not to scale.

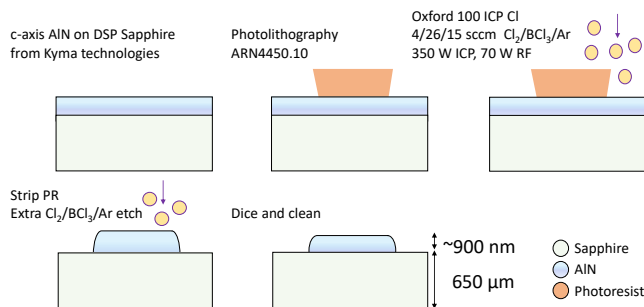


FIG. S2. **Fabrication HBAR chip.** Drawings show a step-by-step process for fabricating our HBAR chip. Not to scale.

TABLE S1. Device parameters readout, transmon and HBAR.

Description	Parameter	Value
Readout resonator frequency	$\omega_r/2\pi$	4.910 GHz
Readout resonator linewidth	$\kappa/2\pi$	2.897 MHz
Resonator Dispersive shift	$\chi/2\pi$	1.2 MHz
Resonator/qubit detuning	Δ	1.07 GHz
Resonator detuning	g_{rq}	81.04 MHz
Qubit transition frequency	$\omega_{eg}/2\pi$	6.067 GHz
Qubit charging energy	E_c/h	260 MHz
Qubit Josephson energy	E_J/h	40.2 GHz
Qubit intrinsic linewidth	$\Gamma/2\pi$	425 kHz
Phonon frequency	$\omega_p/2\pi$	6.064 GHz
Phonon linewidth	$\gamma/2\pi$	6.98 kHz
Phonon - qubit coupling	$g_{qh}/2\pi$	197 kHz

at 4.0/26.0/10.0 sccm, 350 W ICP power, 70 W RF power). After stripping the photoresist, an additional etch step was performed to reduce the thickness of the AlN to ~ 900 nm. Fig. S2 above shows the step-by-step process just described.

Once both chips were fabricated, the HBAR chip was diced into 8x2 mm chips. The smaller HBAR chips were flipped on top of the qubit chip (such that the AlN layer facing down). Using probe needles, the AlN disks were aligned with the transmon antennas. Once aligned, the probe needles were used to hold the chips in position, while a tapered fiber was used to apply two-component epoxy (Loctite EA 3430) on the sides of the top chip. After the epoxy dried, the chip was wire-bonded and mounted in a dilution refrigerator.

II. MEASUREMENT SETUP

All experiments reported in this article were performed on the baseplate of a commercial dilution refrigerator (Triton200-10 Cryofree dilution refrigerator system, Oxford instruments) operating at a base temperature of ~ 20 mK. A schematic of the experimental setup and the external configurations used in the different experiments can be seen in Fig. S3.

The fabricated sample was wire bonded to a PCB, placed on the dilution refrigerator's mixing plate and connected to two coaxial lines. These coaxial lines were used as input/output microwave lines to measure the readout resonators in a capacitively side-coupled transmission configuration.

Outside the dilution refrigerator, coaxial lines connected to a vector network analyzers (VNA, Keysight PNA N5222A, 10MHz-26.5 GHz). Port 1 was employed as a probe signal, port 3 as the qubit drive source and port 2 for readout. For the AC Stark shift experiments, a signal generator was employed (SG, Rohde & Schwarz (SMB 100A, 100 kHz - 12.75 GHz))

For the probe signal, a total estimated attenuation of -108 dB (excluding cable attenuation) was employed. The Qubit drive included a total estimated attenuation of -148 dB (excluding cable attenuation). The Stark signal had a total estimated attenuation of -68 dB (excluding cable attenuation). The high electron mobility transistor (HEMT, LNF-LNC4_8A) has a gain of +44 dB. The room temperature amplifier (RT, MITEQ48, 4-8,07-10p-04) has a gain of +35 dB.

III. DEVICE DETAILS

Table S1 gives the device parameter for the readout resonator (RO), transmon qubit and HBAR resonator.

IV. FULL MASTER EQUATION SIMULATION

In Fig. 3, we show curves corresponding to master equation simulations of the system as well as mean-field modelling. The master equation simulations correspond to numerical solutions of the master equation for the system composed

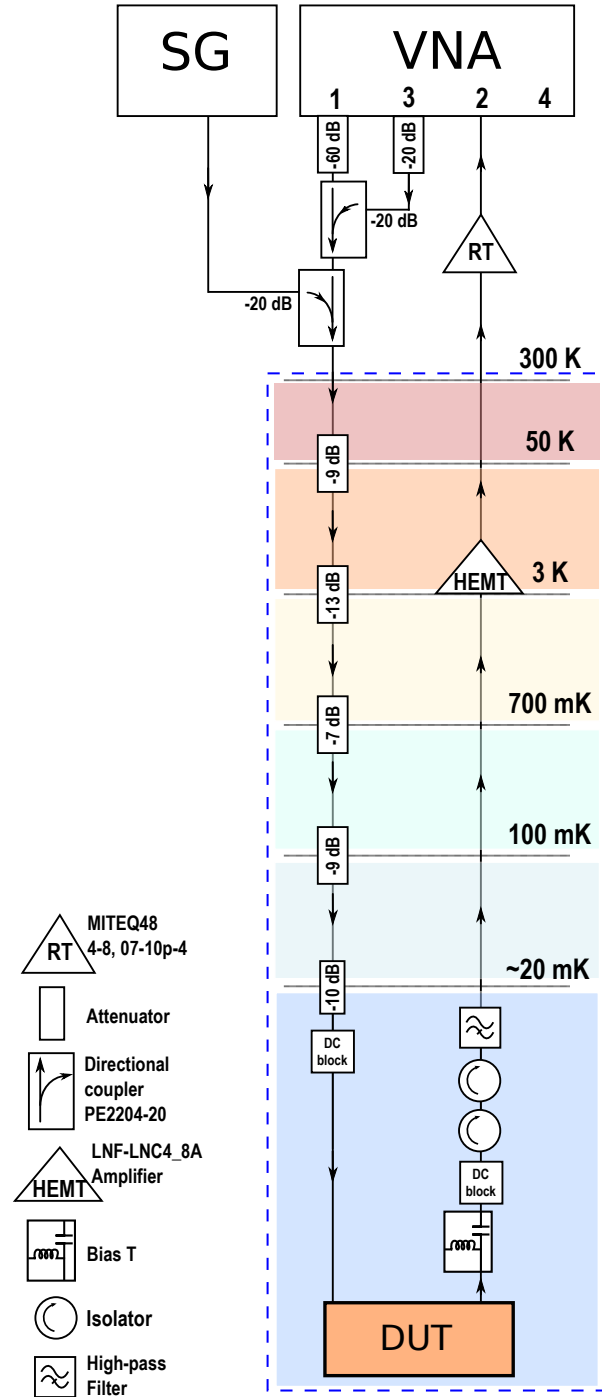


FIG. S3. **Schematic of the measurement setup.** To the right is the general Dilution refrigerator wiring setup. Outside the refrigerator, depicted on the top, we used one setup operated for two measurements. In the configuration on the top, we show our two-tone spectroscopy configuration, including an additional signal generator (SG) to perform AC-Stark shifts on our qubit while performing qubit spectroscopy. We sent a weak continuous wave tone (readout resonator probe) from the vector network analyzer (VNA) port 1 and a second continuous wave tone (qubit drive) from the VNA port 3. These two signals are combined using a directional coupler before entering the dilution refrigerator. The signal from the dilution refrigerator goes through a room-temperature amplifier before it goes to port 2 of the VNA. The drive tone coming from the SG is combined with the two VNA signals using a second directional coupler.

of the resonator, the qubit and the phonon mode, which is given by

$$\begin{aligned} \partial_t \rho = & -\frac{i}{\hbar} [\hat{\mathcal{H}}, \rho] + \gamma \mathcal{L}[\hat{b}] \rho + \kappa \mathcal{L}[\hat{a}] \rho \\ & + \Gamma_1 \mathcal{L}[\hat{\sigma}_-] \rho + \frac{\Gamma_\phi}{2} \mathcal{L}[\hat{\sigma}_z] \rho, \end{aligned} \quad (\text{S1})$$

where Γ_ϕ is the intrinsic qubit dephasing and $\Gamma_1 \sim 2\Gamma$ is the intrinsic qubit relaxation given in term of Γ the intrinsic qubit linewidth (see table S1). The phonon and resonator decay rates are indicated by γ and κ respectively. The superoperator \mathcal{L} indicates the standard dissipator:

$$\mathcal{L}[\hat{o}] \rho = \hat{o} \rho \hat{o}^\dagger - \frac{1}{2} \{ \hat{o}^\dagger \hat{o}, \rho \}. \quad (\text{S2})$$

The Hamiltonian $\hat{\mathcal{H}}$ describes a Jaynes-Cummings coupling between the phonon mode and the qubit, and a dispersive coupling between the qubit and the resonator:

$$\begin{aligned} \frac{\hat{\mathcal{H}}}{\hbar} = & -\Delta_b \hat{b}^\dagger \hat{b} - \frac{\Delta_q}{2} \hat{\sigma}_z - \Delta_r \hat{a}^\dagger \hat{a} \\ & + \chi \hat{a}^\dagger \hat{a} \hat{\sigma}_z + g_{\text{qh}} \left(\hat{b} \hat{\sigma}_+ + \hat{b}^\dagger \hat{\sigma}_- \right) \\ & + \varepsilon_d (\hat{\sigma}_+ + \hat{\sigma}_-) + \varepsilon_p (\hat{a}^\dagger + \hat{a}). \end{aligned} \quad (\text{S3})$$

The above Hamiltonian is written in a frame rotating at the drive frequency ω_d . The operators $\hat{\sigma}_z$ and $\hat{\sigma}_\pm$ correspond to the standard Pauli operators, while \hat{a} and \hat{b} correspond to the resonator and the phonon mode annihilation operators. The phonon-drive detuning is $\Delta_b = \omega_d - \omega_p$, the resonator-drive detuning is $\Delta_r = \omega_d - \omega_r$ (already including the Lamb shift), and the qubit-drive detuning is $\Delta_q = \omega_d - \omega_{\text{eg}}$. The qubit-resonator dispersive coupling rate is indicated by χ and the phonon-qubit coupling by g_{qh} (see table S1). The resonator drive amplitude is ε_p and the (weak) qubit drive amplitude is ε_d .

To obtain the red curve shown in Fig. 3 of the main text, we numerically solve the master equation using the Python package `qutip` and compute the normalized steady-state qubit population as a function of the phonon-drive detuning. The same behavior can be obtained by the procedure outlined in the next section for the mean-field calculations: e.g. by considering the dynamics for an initial density matrix $\hat{\sigma}_+ \rho_s$, where ρ_s is the steady-state of S1, and then evaluating the Fourier transform of the expectation value $\langle \hat{\sigma}_- \rangle(t)$.

V. MEAN-FIELD CALCULATION OF THE QUBIT SPECTRUM

The dynamics of the system can also be described using an effective mean-field approach. The starting point is an effective master equation describing the temporal evolution of the qubit-phonon density matrix ϱ , obtained in [28]:

$$\begin{aligned} \partial_t \varrho = & -\frac{i}{\hbar} [\hat{\mathcal{H}}_{\text{eff}}, \varrho] + \gamma \mathcal{L}[\hat{b}] \varrho \\ & + \Gamma_1 \mathcal{L}[\hat{\sigma}_-] \varrho + \frac{\tilde{\Gamma}_\phi}{2} \mathcal{L}[\hat{\sigma}_z] \varrho. \end{aligned} \quad (\text{S4})$$

Such a master is obtained by starting with the dynamics of the system in the dispersive cavity-qubit limit, given by the master equation in Eq. (S1), and then eliminating the cavity dynamics using a procedure akin to the one in [37]. The cavity dynamics induces a qubit dephasing and frequency shift, included in the effective Hamiltonian $\hat{\mathcal{H}}_{\text{eff}}$ and in the qubit dephasing $\tilde{\Gamma}_\phi$. The effective qubit-phonon Hamiltonian, in a frame rotating at the cavity drive frequency ω_d , is given by

$$\begin{aligned} \frac{\hat{\mathcal{H}}_{\text{eff}}}{\hbar} = & -\Delta_b \hat{b}^\dagger \hat{b} - \frac{\tilde{\Delta}_q}{2} \hat{\sigma}_z + g_{\text{qh}} \left(\hat{b} \hat{\sigma}_+ + \hat{b}^\dagger \hat{\sigma}_- \right) \\ & + \varepsilon_d (\hat{\sigma}_+ + \hat{\sigma}_-), \end{aligned} \quad (\text{S5})$$

The effective dephasing and frequency shift are given by

$$\begin{aligned} \tilde{\Gamma}_\phi &= \Gamma_\phi + \Gamma_{\phi, \text{cav}}(t), \\ \tilde{\Delta}_q &= \Delta_q - \omega_{\text{q, cav}}(t), \\ \omega_{\text{q, cav}}(t) &= 2\chi \text{Re}[\alpha_g(t) \alpha_e^*(t)], \\ \Gamma_{\phi, \text{cav}}(t) &= 2\chi \text{Im}[\alpha_g(t) \alpha_e^*(t)]. \end{aligned} \quad (\text{S6})$$

In the above expressions, $\alpha_{g,e}$ are the microwave cavity occupancies provided that the qubit is in the ground (g) or excited (e) state; they are given by

$$\begin{aligned}\partial_t \alpha_e &= \left[i(\Delta_r - \chi) - \frac{\kappa}{2} \right] \alpha_e - i\epsilon_p, \\ \partial_t \alpha_g &= \left[i(\Delta_r + \chi) - \frac{\kappa}{2} \right] \alpha_g - i\epsilon_p,\end{aligned}\tag{S7}$$

From the effective master equation (S4), we obtain the following set of equations for the expectation values $\langle \hat{b} \rangle = b$, $\langle \hat{\sigma}_- \rangle = s_-$, $\langle \hat{\sigma}_z \rangle = s_z$:

$$\begin{aligned}\partial_t b &= \left(i\Delta_b - \frac{\gamma}{2} \right) b(t) - ig_{qh} s_-(t), \\ \partial_t s_- &= \left(i\tilde{\Delta}_q - \tilde{\Gamma} \right) s_-(t) + ig_{qh} b(t) s_z(t), \\ \partial_t s_z &= 2is_-(t) (g_{qh} b^*(t) + \varepsilon_d) - 2is_-^*(t) (g_{qh} b(t) + \varepsilon_d) \\ &\quad - \Gamma_1 (s_z(t) + 1),\end{aligned}\tag{S8}$$

which assume the mean field approximations $\langle \hat{b} \hat{\sigma}_z \rangle \approx \langle \hat{b} \rangle \langle \hat{\sigma}_z \rangle = bs_z$ and $\langle \hat{b}^\dagger \hat{\sigma}_- \rangle \approx \langle \hat{b}^\dagger \rangle \langle \hat{\sigma}_- \rangle = b^* s_-$. We have defined the total qubit linewidth $\tilde{\Gamma} = \tilde{\Gamma}_\varphi + \Gamma_1/2$

The qubit spectrum shown in Fig. 3 of the main text is obtained by numerically solving the set of coupled equations (S8) with appropriate initial conditions. For that, we recall that the qubit spectrum is given by [31]

$$\begin{aligned}S(\omega) &= \frac{1}{2\pi} \int_{-\infty}^{\infty} dt e^{i\omega t} \langle \hat{\sigma}_-(t) \hat{\sigma}_+(0) \rangle_s \\ &= \frac{1}{\pi} \text{Re} \left[\int_0^{\infty} dt e^{i\omega t} \langle \hat{\sigma}_-(t) \hat{\sigma}_+(0) \rangle_s \right],\end{aligned}\tag{S9}$$

where $\langle \cdot \rangle_s = \text{Tr}[\cdot \varrho_s]$, is the expectation value of an operator in the steady-state ϱ_s . We notice then that

$$\langle \hat{\sigma}_-(t) \hat{\sigma}_+(0) \rangle_s = \text{Tr}[\hat{\sigma}_- \varrho_I(t)],\tag{S10}$$

where $\varrho_I(t)$ is the temporal evolution of a state initially in $\hat{\sigma}_+ \varrho_s$. Considering the steady-state of the system under a weak qubit drive, which we have studied in detail in [28], we have the following initial conditions for (S8)

$$\begin{aligned}b(0) &= \langle \hat{b} \hat{\sigma}_+ \rho_s \rangle = 0, \\ s_-(0) &= \langle \hat{\sigma}_- \hat{\sigma}_+ \rho_s \rangle = 1, \\ s_z(0) &= \langle \hat{\sigma}_z \hat{\sigma}_+ \rho_s \rangle = 0.\end{aligned}\tag{S11}$$

The qubit spectrum is then obtained by the Fourier transform of $s_-(t)$. To obtain the fit parameters given in the main text, we have used standard Python libraries for data fit using the qubit absorption spectrum calculated as explained above.

VI. REFERENCE QUBIT MEASUREMENTS

As a reference, a nominally identical qubit was measured without an HBAR to determine the contribution of the qubit decoherence resulting from the coupling to the HBAR. Performing a fit of the qubit spectrum [38] yields a qubit linewidth $\Gamma = 2\pi \times 1.9$ MHz. As a representative qubit, this is quite a bit worse than the value used in the main text, suggesting the coherence limitation of the qubit is indeed unrelated to the piezoelectric material.

Indeed, recent work has identified that the SF₆ etch step is the leading contributor to the qubit decoherence. The original etch has been replaced by a two-step process; the NbTiN was first etched using a SF₆ dry etch through approximately ninety percent of its thickness, leaving a thin layer of metal. The remaining metal was removed using an RCA 1 wet etch; NH₃OH/H₂O₂/H₂O (1:1:5) heated to 40°C. This modification to the fabrication recipe has resulted in recent qubits with T₁ decoherence times on the order of 30 μs.

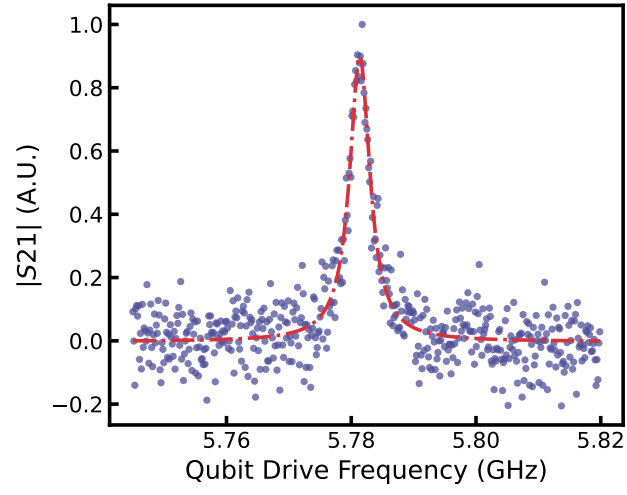


FIG. S4. **Reference qubit two-tone spectroscopy.** Two-tone spectroscopy of a reference qubit.